Molecular dynamics simulations of tethered membranes with periodic boundary conditions

Z. Zhang and H. T. Davis
Department of Chemical Engineering and Materials Science, University of Minnesota, Minneapolis, Minnesota 55455

D. M. Kroll
Department of Medicinal Chemistry and Minnesota Supercomputer Institute, University of Minnesota, Minneapolis, Minnesota 55455

(Received 30 August 1995)

Tethered membranes with periodic boundary conditions are studied using constant temperature-pressure molecular dynamics techniques. Constraint and Nosé thermostating are used in conjunction with Andersen and Cleveland-Wentzcovitch constant pressure algorithms. In contrast to earlier work, it is found that the scaling behavior is consistent with the most accurate previous simulation studies (of tethered vesicles). The Poisson ratio for these networks is determined to be $\sigma_P = -0.15 \pm 0.01$. The relative efficiency of the various algorithms is also discussed.

PACS number(s): 64.60.Fr, 05.40.+j, 82.65.Dp

I. INTRODUCTION

Tethered or solidlike membranes have been extensively studied recently [1], and we now have a rather complete picture of their thermal properties. Unlike linear polymers, two-dimensional tethered networks are known to exhibit a flat phase with broken orientational symmetry. Out-of-plane thermal undulations that induce a nonzero local Gaussian curvature are strongly suppressed because they are accompanied by in-plane shear deformations. As a result, even "phantom"—self-intersecting— tethered membranes should be flat at low temperatures. Excluded volume interactions appear to stabilize the flat phase at all temperatures.

There are several experimental realizations of solid membranes. These include metal dichalcogenide layers [2], polymerized adsorbed monolayers [3], mammalian red blood cell cytoskeletons [4], two-dimensional polymers of chiral precursors [5], and suspended layers of graphitic oxide in aqueous solution [6, 7]. A major difficulty is finding elastic networks of appropriate size with a sufficiently small width to thickness aspect ratio. The best studied systems are two-dimensional sheets of graphite oxide suspended in aqueous solution, since micron size sheets with a thickness on the order of 10 Å can be formed by exfoliating carbon with a strong oxidizing agent. Whereas the original light scattering experiments on suspended membranes of graphite oxide were consistent with a fractal dimension of 2.5 [6], suggesting a crumpled phase, subsequent freeze-fracture electron microscopy and static light scattering experiments indicate that they are in reality flat [7].

This flat phase is characterized by anomalous elastic behavior, with wave-vector-dependent in-plane elastic constants $\lambda_R(q) \sim \mu_R(q) \sim q^{2(1-\eta)}$ and renormalized bending rigidity $\kappa_R(q) \sim q^{-\eta}$ [8]. For a flat crystalline network, the rms amplitude of the out-of-plane fluctuations, $\sqrt{\langle z^2 \rangle}$, is related to the in-plane length scale, L, by $\sqrt{\langle z^2 \rangle} \sim L^{\zeta}$, with $\zeta = 1 - \eta/2$. There is as yet no clear consensus concerning the precise value of the exponent ζ. Early simulations performed using bead-spring models with free edge boundary conditions yielded the estimate $\zeta = 0.64 \pm 0.04$. However, Abraham [9] pointed out that this value for ζ may be too large due to edge fluctuations. To eliminate edge effect, Abraham simulated a tensionless network with periodic boundary conditions, and obtained a roughness exponent $\zeta \approx 0.53$. The best theoretical estimate, $\zeta \approx 0.59$, was obtained by Le Doussal and Radzhihovsky [10] using a self-consistent screening approximation.The results of recent simulations of tethered vesicles [11, 12] are in good agreement with this result. Another, currently untested, prediction of [10] is that the two-dimensional Poisson ratio $\sigma_P = \lambda(q = 0)/[\lambda(q = 0) + 2\mu(q = 0)]$ of these networks is a universal number, equal to $-1/3$.

The purpose of this paper is to help resolve these conflicting results and determine the Poisson ratio σ_P. We have performed constant temperature-pressure molecular dynamics (MD) simulations of tensionless tethered membranes with periodic boundary conditions using three different algorithms that can be proven to generate configurations belonging to the isothermal-isobaric ensemble. We find a roughness exponent $\zeta \approx 0.59$, in excellent agreement with the results of both the self-consistent screening approximation and simulations of tethered vesicles [11, 12]. The in-plane elastic constants are determined, and it is shown that the Poisson ratio $\sigma_P = -0.15 \pm 0.01$. These results indicate that the self-consistent screening approximation yields extremely accurate results for the scaling exponents, but that the predicted Poisson ratio is probably too negative. The relative efficiency of various algorithms for performing isothermal-isobaric simulations are also discussed in this paper.

II. SIMULATION METHODS AND MODEL

There has been considerable progress in extending MD methods to simulate ensembles other than the traditional microcanonical ensemble. In this regard, Andersen's introduction of the constant pressure MD method represented a significant breakthrough [13]. In this method, the volume becomes a dynamical variable and is allowed to fluctuate. The average volume is determined by the balance between the internal pressure and the externally set pressure p. The enthalpy of the systems is approximately conserved so that his method generates the constant enthalpy, constant pressure (H,p,N) ensemble. The procedure guarantees that the averages of static quantities are equal to those in the isoenthalpic-isobaric ensemble. Subsequently, Nosé [14] introduced an analogous procedure for performing MD simulations at constant temperature. In this method, an additional degree of freedom, s, is introduced in order to allow the total energy of the system to fluctuate. A special choice of the potential for the variable s guarantees that the averages of static quantities generated are equal to those in the canonical ensemble. The thermostating procedure originally proposed by Hoover *et al.* [15, 16] and Evans [17] (which we call constraint thermostating) can be derived from this method by imposing an additional constraint. Either of these methods is easily combined to allow MD simulation in the isothermal-isobaric ensemble.

Subsequently, several generalizations of Andersen's method have been introduced which allow both the size and shape of the MD cell to fluctuate. In this paper, we employ the Lagrangians suggested in Refs. [18] and [19]. In contrast to the method first suggested by Parrinello and Rahman [20], the Lagrangian we employ is invariant with respect to the choice of the simulation cell basis vectors and reduces to Andersen's Lagrangian in the limit of isoshape fluctuations.

The networks we consider consist of $N = L \times L$ particles of mass m tethered in a triangular array. The particles interact through the shifted and truncated Lennard-Jones potential

$$U_{LJ} = \begin{cases} 4\epsilon[(\frac{\sigma}{r})^{12} - (\frac{\sigma}{r})^6 + \frac{1}{4}] & \text{for } r \le 2^{1/6}\sigma \\ 0 & \text{for } r > 2^{1/6}\sigma. \end{cases} \quad (1)$$

This purely repulsive potential represents the excluded volume interactions. We take U_{LJ} only between nearest- and next-nearest neighbors; this simplifies the calculation considerably while still ensuring that the network does not self-intersect [21]. There is an additional finitely extensible nonlinear elastic (FENE) potential between tethered (nearest-neighbor) particles of the form

$$U_{FENE} = \begin{cases} -0.5kR_0{}^2 \ln[1 - (r/R_0)^2] & \text{for } r \le R_0 \\ \infty & \text{for } r > R_0. \end{cases} \quad (2)$$

We take $k = 6\epsilon/\sigma^2$ and $R_0 = 1.5\sigma$. In the following, length, mass, and energy are given in units of σ, m, and ϵ, respectively. Our unit of time is $\tau = \sigma(m/\epsilon)^{1/2}$.

We have performed isothermal MD simulations of tensionless (spreading pressure $p = 0$) tethered membranes with periodic boundary conditions using three methods: (1) Constraint thermostating with Andersen's constant-pressure algorithm (CA), (2) Nosé thermostating with Andersen's constant-pressure algorithm (NA), and (3) Nosé thermostating with Cleveland-Wentzcovitch constant-pressure algorithm (NCW). In methods (1) and (2), the shape of the simulation cell is fixed, and the lengths of the two basis vectors spanning the cell are equal. In this case, only the area A of the simulation cell fluctuates. In method (3), both the size and shape of the cell are allowed to fluctuate, and the dynamics of the simulation cell is described by an equation of motion for the matrix $\mathbf{h}$ of cell basis vectors. In all cases, the simulations are performed at zero spreading pressure, $p = 0$, and constant temperature, $k_BT = \epsilon$.

A. Constraint-Andersen (CA) algorithm

In the two-dimensional version of Andersen's constant-pressure molecular dynamics method, we decompose the coordinate vectors $\{\mathbf{r}_i\}$ of the particles into their in-plane components $\boldsymbol{\rho}$ and out-of-plane components z, so that $\mathbf{r}_i = (\boldsymbol{\rho}_i, z_i)$. The coordinates $\boldsymbol{\rho}_i$, $i = 1,\ldots,N$ of the particles are then replaced by scaled coordinate vectors $\mathbf{s}_i$ defined by [13]

$$\mathbf{s}_i \equiv \boldsymbol{\rho}_i/A^{1/2}, \quad (3)$$

where A is the (projected) area of the network. The Lagrangian of the system is

$$\mathcal{L}_A = \frac{1}{2}m\sum_{i=1}^{N}[A\,\dot{\mathbf{s}}_i\cdot\dot{\mathbf{s}}_i + \dot{z}_i^2] - \sum_{i=1}^{N}\sum_{j>i}\phi(r_{ij}) + \frac{Q_A}{2}\dot{A}^2 - pA,$$

where Q_A is a "mass" for the area motion and ϕ is the interparticle potential. Q_A determines the relaxation time for an imbalance between the external pressure and the internal stress. We have chosen Q_A to make this relaxation time on the order of L/c, where L is the MD cell size and c is the sound velocity. The exact choice of Q_A is not critical, however, and in fact, the equilibrium properties of the system are independent of the choice of Q_A. The Euler-Lagrange equations of motion are

$$\ddot{\mathbf{s}}_i = -\frac{1}{m}\sum_{i\neq j}\frac{\phi'(r_{ij})}{r_{ij}}\mathbf{s}_{ij} - \dot{\mathbf{s}}_i\dot{A}/A, \quad (4a)$$

$$\ddot{z}_i = -\frac{1}{m}\sum_{i\neq j}\frac{\phi'(r_{ij})}{r_{ij}}z_{ij}, \quad (4b)$$

and

$$\ddot{A} = (P_s - p)/Q_A, \quad (4c)$$

where P_s is the virial pressure

$$P_s = \frac{1}{2A}\left[m\sum_{i=1}^{N}\mathbf{v}_i\cdot\mathbf{v}_i - \sum_{i=1}^{N}\sum_{j>i}\frac{\phi'(r_{ij})}{r_{ij}}\rho_{ij}^2\right], \quad (5)$$

with $\mathbf{v}_i = A^{1/2}\dot{\mathbf{s}}_i$. Expressed in terms of the momentum $\mathbf{p}_i = m\{\mathbf{v}_i, \dot{z}_i\}$, Eqs. (4a) and (4b) are

$$\dot{\mathbf{p}}_i = -\sum_{i\neq j}\frac{\phi'(r_{ij})}{r_{ij}}\mathbf{r}_{ij} - \frac{1}{2}\mathbf{p}_i\dot{A}/A \quad (6a)$$

for the x and y components, and

$$\dot{\mathbf{p}}_i = -\sum_{i\neq j}\frac{\phi'(r_{ij})}{r_{ij}}\mathbf{r}_{ij} \quad (6b)$$

for the z component. In order to simulate at constant temperature T, we have implemented the damped force, or constraint, method described in Refs. [15–17, 22]. In this method, damping terms $-\zeta\mathbf{p}_i/m$ are added to the right-hand side (rhs) of Eqs. (6a) and (6b), and ζ is determined from the condition that the time derivative of the temperature,

$$T = \frac{1}{3(N-1)k_B}\sum_{i=1}^{N}\mathbf{p}_i\cdot\mathbf{p}_i, \quad (7)$$

is zero. This implies that

$$\zeta = \sum_{i=1}^{N}\mathbf{p}_i\cdot\left[-\sum_{i\neq j}\frac{\phi'(r_{ij})}{r_{ij}}\mathbf{r}_{ij} - \frac{m}{2}\mathbf{v}_i\dot{A}/A\right]\Bigg/\sum_{i=1}^{N}\mathbf{p}_i\cdot\mathbf{p}_i. \quad (8)$$

The factor $N-1$ instead of N occurs in Eq. (7) since three degrees of freedom have been removed by the constraint of zero total linear momentum. These equations of motion were integrated using the leap-frog version of the Verlet algorithm as implemented in [22] using $Q_A = 0.1$ and a time step of 0.008τ. System sizes $N = 100$, 196, 400, 784, and 1600 were studied. After equilibration, averages were taken over at least 20 million timesteps.

B. Nosé-Andersen (NA) algorithm

Nosé thermostating requires the introduction of a new degree of freedom, s, and a virtual, or scaled, time variable t. t is related to the real, or actual, time t' by

$$t' = \int^t dt/s, \quad (9)$$

so that $dt' = dt/s$. The dynamics of the system are described by the effective Lagrangian

$$\mathcal{L}_1 = \frac{1}{2}Q_s\dot{s}^2 - gk_BT\ln(s) + \frac{s^2}{2}m\sum_{i=1}^{N}[A\,\dot{\mathbf{s}}_i\cdot\dot{\mathbf{s}}_i + \dot{z}_i^2] - \sum_{i=1}^{N}\sum_{j>i}\phi(r_{ij}) + \frac{Q_A}{2}\dot{A}^2 - pA, \quad (10)$$

where Q_A and Q_s are "masses" controlling the dynamics of A and s, respectively. $gk_BT\ln(s)$ is a potential energy associated with the variable s; g is related to the number of degrees of freedom of the system, k_B is Boltzmann's constant, and T is the externally set value of the temperature. The logarithmic dependence of this potential on s is essential for producing the canonical ensemble [12, 14, 23]. The most efficient choice for Q_s is one that makes the characteristic time scale for s to be on the order of the time it takes for a sound wave to travel the nearest-neighbor distance [23]. Because we sample in virtual time and we fix the center-of-mass momenta to be zero, $g = 3N - 2$ [23].

The Euler-Lagrange equations of motion are

$$\ddot{\mathbf{s}}_i = -\frac{1}{ms^2}\sum_{i\neq j}\frac{\phi'(r_{ij})}{r_{ij}}\mathbf{s}_{ij} - \dot{\mathbf{s}}_i\dot{A}/A - 2\dot{s}\dot{\mathbf{s}}_i/s, \quad (11a)$$

$$\ddot{z}_i = -\frac{1}{ms^2}\sum_{i\neq j}\frac{\phi'(r_{ij})}{r_{ij}}z_{ij} - 2\dot{s}\dot{z}_i/s, \quad (11b)$$

$$\ddot{s} = \left[ms^2\sum_{i=1}^{N}\{A\,\dot{\mathbf{s}}_i\cdot\dot{\mathbf{s}}_i + \dot{z}_i^2\} - gk_BT\right]\Big/(Q_s s), \quad (11c)$$

and

$$\ddot{A} = (P_s - p)/Q_A, \quad (11d)$$

where P_s is the virial pressure

$$P_s = \frac{1}{2A}\left[ms^2\sum_{i=1}^{N}\mathbf{v}_i\cdot\mathbf{v}_i - \sum_{i=1}^{N}\sum_{j>i}\frac{\phi'(r_{ij})}{r_{ij}}\rho_{ij}^2\right], \quad (12)$$

where $\mathbf{v}_i = A^{1/2}\dot{\mathbf{s}}_i$, and dots represent derivatives with respect to the *virtual* time t. Expressed in terms of the physical coordinates $\boldsymbol{\rho}_i$, Eq. (11a) becomes

$$\ddot{\boldsymbol{\rho}}_i = -\frac{1}{ms^2}\sum_{i\neq j}\frac{\phi'(r_{ij})}{r_{ij}}\boldsymbol{\rho}_{ij} - 2\frac{\dot{s}\dot{\boldsymbol{\rho}}_i}{s} + \frac{\boldsymbol{\rho}_i}{2}\left[\frac{\ddot{A}}{A} - \frac{1}{2}\left(\frac{\dot{A}}{A}\right)^2 + 2\frac{\dot{A}\dot{s}}{As}\right]. \quad (13)$$

In the NA procedure, the dynamics is described by Eqs. (11b)–(11d) and (13).

Since first-order time derivatives appear on the rhs of the equations of motion, we have used a third-order predictor-corrector algorithm to integrate these equations. Very small integration time steps Δt in the range 0.001τ–0.002τ were used, with smaller values of Δt for larger system sizes. Even then, we found it necessary to iterate the corrector step in order to prevent a drift in the variable $s(t)$. We utilized the following procedure: the forces due to interparticle interactions are calculated once using the predicted value of the coordinates. These forces, together with other predicted values, are then used to get corrected values for coordinates and their

time derivatives. This procedure is iterated four times, using the interparticle forces calculated after the first predictor step. This procedure is significantly faster than a full corrector iteration because the interparticle forces are calculated only once per time step. We have found that this procedure removes the drift in the variable $s(t)$ and significantly increases the accuracy of this integration scheme. Simulations were performed using Q_A and Q_s in the ranges $0.1-0.35$ and $5-14$, respectively. System sizes $N = 100$, 196, 400, and 784 were studied, and averages were taken over at least 40 million time steps.

C. Nosé-Cleveland-Wentzcovitch (NCW) algorithm

In this case, both the size and the shape of the simulation cell are allowed to fluctuate. The simulation cell configuration is described by the matrix $\mathbf{h}$ of the two vectors $\mathbf{a}$ and $\mathbf{b}$ that span the edges of the cell. If $\mathbf{h}$ is defined to be the matrix with columns $\mathbf{a}$ and $\mathbf{b}$, the area of the MD cell is $A = \det\{\mathbf{h}\}$. The position of a particle in the cell is

$$\boldsymbol{\rho}_i = \mathbf{h}\mathbf{s}_i = \xi_i \mathbf{a} + \eta_i \mathbf{b}, \tag{14}$$

with $0 \le \xi_i, \eta_i \le 1$ and the square of the distance between particles i and j is $r_{ij}^2 = \rho_{ij}^2 + z_{ij}^2$, where

$$\rho_{ij}^2 = \mathbf{s}_{ij}^T \mathbf{G} \mathbf{s}_{ij} \ , \tag{15}$$

with the metric tensor $\mathbf{G} = \mathbf{h}^T\mathbf{h}$. When Nosé thermostating is combined with Cleveland and Wentzcovitch constant pressure methods, the Lagrangian is

$$\mathcal{L}_2 = \frac{1}{2}Q_s\dot{s}^2 - gk_BT\ln(s) + \frac{ms^2}{2}\sum_{i=1}^{N}[\dot{\mathbf{s}}_i^T\mathbf{G}\dot{\mathbf{s}}_i + \dot{z}_i^2] - \sum_{i=1}^{N}\sum_{j>i}\phi(r_{ij}) + \frac{Q_{CW}}{2}\mathrm{Tr}(\dot{\mathbf{h}}\boldsymbol{\sigma}^T\boldsymbol{\sigma}\dot{\mathbf{h}}^T) - pA, \tag{16}$$

and the equations of motion are

$$\ddot{\mathbf{s}}_i = -\frac{1}{ms^2}\sum_{i\neq j}\frac{\phi'(r_{ij})}{r_{ij}}\mathbf{s}_{ij} - \mathbf{G}^{-1}\dot{\mathbf{G}}\dot{\mathbf{s}}_i - 2\dot{s}\dot{\mathbf{s}}_i/s, \tag{17a}$$

$$\ddot{z}_i = -\frac{1}{ms^2}\sum_{i\neq j}\frac{\phi'(r_{ij})}{r_{ij}}z_{ij} - 2\dot{s}\dot{z}_i/s, \tag{17b}$$

$$\ddot{s} = \left[ms^2\sum_{i=1}^{N}[\dot{\mathbf{s}}_i^T\mathbf{G}\dot{\mathbf{s}}_i + \dot{z}_i^2] - gk_BT\right] \Big/ (Q_s s), \tag{17c}$$

and

$$\ddot{\mathbf{h}} = \frac{1}{Q_{CW}A}(\boldsymbol{\Pi} - p\mathbf{1})\mathbf{h} + \left\{-2\frac{\dot{A}}{A}\dot{\mathbf{h}} + \frac{1}{A^2}\mathrm{Tr}(\dot{\mathbf{h}}\mathbf{f}\dot{\mathbf{h}}^T)\mathbf{h} + \dot{\mathbf{h}}\mathbf{h}^{-1}\dot{\mathbf{h}} + \frac{1}{A^2}(\dot{\mathbf{h}}\mathbf{f}\dot{\mathbf{h}}^T - \boldsymbol{\sigma}\dot{\mathbf{h}}^T\dot{\mathbf{h}}\boldsymbol{\sigma}^T)\mathbf{h}\right\}, \tag{17d}$$

where $\boldsymbol{\sigma} = A(\mathbf{h}^T)^{-1}$, $\mathbf{f} = \boldsymbol{\sigma}^T\boldsymbol{\sigma}$, and $\boldsymbol{\Pi}$ is the stress tensor

$$\boldsymbol{\Pi} = \frac{ms^2}{A}\sum_{i=1}^{N}\mathbf{p}_i\mathbf{p}_i^T - \frac{1}{A}\sum_{i=1}^{N}\sum_{j>i}\frac{\phi'(r_{ij})}{r_{ij}}\boldsymbol{\rho}_{ij}\boldsymbol{\rho}_{ij}^T, \tag{18}$$

with $\mathbf{p}_i = \mathbf{h}\dot{\mathbf{s}}_i$. The equation of motion in Cartesian space is

$$\ddot{\boldsymbol{\rho}}_i = \ddot{\mathbf{h}}\mathbf{h}^{-1}\boldsymbol{\rho}_i - \frac{1}{ms^2}\sum_{i\neq j}\frac{\phi'(r_{ij})}{r_{ij}}\boldsymbol{\rho}_{ij} + \left[\frac{1}{A}\{\dot{\mathbf{h}}\boldsymbol{\sigma}^T - \boldsymbol{\sigma}\dot{\mathbf{h}}^T\} - 2\frac{\dot{s}}{s}\right]\left[\dot{\boldsymbol{\rho}}_i - \frac{1}{A}\dot{\mathbf{h}}\boldsymbol{\sigma}^T\boldsymbol{\rho}_i\right]. \tag{19}$$

The equations of motion (17b)–(17d) and (19) were integrated using the third-order predictor-corrector method described in Sec. II B. Time steps Δt in the range $0.001\tau - 0.002\tau$ were used. $g = 3N - 2$, and values for Q_A and Q_s were chosen in the ranges $0.3 - 1$ and $5 - 14$, respectively. System sizes $N = 100$, 196, 400, and 784 were simulated, and averages were taken over at least 100 million time steps.

III. ELASTIC PROPERTIES

The elastic compliance tensor

$$S_{ijkl} = -\frac{\lambda}{4\mu(\mu+\lambda)}\delta_{ij}\delta_{kl} + \frac{1}{4\mu}(\delta_{ik}\delta_{jl} + \delta_{il}\delta_{jk}) \tag{20}$$

is related to the thermally induced strain correlations by

$$\mathcal{A}\langle\epsilon_{ij}\epsilon_{kl}\rangle = k_BTS_{ijkl}, \tag{21}$$

where $\mathcal{A}$ is the (projected) area of the network. The strain tensor is given by [20]

$$\boldsymbol{\epsilon} = \frac{1}{2}\left[(\mathbf{h}_0^T)^{-1}\mathbf{G}\ \mathbf{h}_0^{-1} - \mathbf{1}\right], \tag{22}$$

where $\mathbf{1}$ is the unit matrix and the matrix of reference basis vectors $\mathbf{h}_0$ is determined by the requirement $\langle\boldsymbol{\epsilon}\rangle = \mathbf{0}$. Using (20) and (21), one finds that

$$\langle\epsilon_{11}\epsilon_{22}\rangle = -\frac{k_BT}{\langle A\rangle}\frac{\lambda}{4\mu(\lambda+\mu)} \ , \tag{23a}$$

$$\langle\epsilon_{12}\epsilon_{12}\rangle = \frac{k_BT}{\langle A\rangle}\frac{1}{4\mu} \ , \tag{23b}$$

and

$$\langle\epsilon_{11}\epsilon_{11}\rangle = \langle\epsilon_{22}\epsilon_{22}\rangle = \frac{k_BT}{\langle A\rangle}\frac{\lambda+2\mu}{4\mu(\lambda+\mu)} \ , \tag{23c}$$

where $\langle A\rangle = \det\{\mathbf{h}_0\}$. Note that these three strain correlation functions are not independent, but fulfill the relation

$$\langle\epsilon_{11}\epsilon_{11}\rangle - \langle\epsilon_{11}\epsilon_{22}\rangle = 2\langle\epsilon_{12}\epsilon_{12}\rangle. \tag{24}$$

Finally, to leading order in $\boldsymbol{\epsilon}$, the area susceptibility, $K_A \equiv [\langle A^2\rangle - \langle A\rangle^2]/\langle A\rangle$, is given by

$$K_A/\langle A\rangle = \langle\ [\mathrm{Tr}\ \boldsymbol{\epsilon}]^2\ \rangle \ , \tag{25}$$

so that

$$K_A = \frac{k_B T}{(\lambda + \mu)} \ . \tag{26}$$

The two-dimensional Poisson ratio $\sigma_P = \lambda/(\lambda + 2\mu)$ can be expressed in terms of ratios of these strain correlation functions. We have used the following ratios to estimate σ_P:

$$\sigma_P^{(1)} = -\langle \epsilon_{11}\epsilon_{22} \rangle / \langle \epsilon_{11}\epsilon_{11} \rangle \ , \tag{27a}$$

$$\sigma_P^{(2)} = -1 + 2\langle \epsilon_{12}\epsilon_{12} \rangle / \langle \epsilon_{11}\epsilon_{11} \rangle \ , \tag{27b}$$

and

$$\sigma_P^{(3)} = 1 - K_A / [2\langle A \rangle \langle \epsilon_{11}\epsilon_{11} \rangle] \ . \tag{27c}$$

Since (27b) is equivalent to (27a) because of (24), the difference between $\sigma_P^{(1)}$ and $\sigma_P^{(2)}$ is a measure of the statistical accuracy of our data. Since we have calculated K_A using $A = \det\{\mathbf{h}\}$, our result for the area compressibility contains contributions from higher-order strain correlation functions, and is therefore not equivalent to expression (25). The difference between $\sigma_P^{(3)}$ and the other two estimates for the Poisson ratio is a measure of the size of these higher-order contributions.

In order to determine the strain correlation functions, it is convenient to express the elements of the strain tensor in terms of the basis vectors $\{\mathbf{a}, \mathbf{b}\}$ of the MD cell. Choosing the x axis to coincide with the direction of $\mathbf{a}$, one finds

$$\epsilon_{11} = (\mathbf{a}^2/c^2 - 1)/2 \ , \tag{28a}$$

$$\epsilon_{12} = \epsilon_{21} = \mathbf{a} \cdot \mathbf{g}/(2c^2) \ , \tag{28b}$$

and

$$\epsilon_{22} = (\mathbf{g}^2/c^2 - 1)/2, \tag{28c}$$

where $\mathbf{g} \equiv (2\mathbf{b} - \mathbf{a})/\sqrt{3}$. The equilibrium length, c, of the cell edge is defined by the thermal averages $c^2 \equiv \langle \mathbf{a}^2 \rangle = \langle \mathbf{b}^2 \rangle = \langle \mathbf{g}^2 \rangle$, and the angle between the mean directions of the two basis vectors is $\pi/3$. Since the shape of the simulation cell is fixed in both the CA and NA methods,

$$\epsilon_{11} = \epsilon_{22} = (\mathbf{a}^2/c^2 - 1)/2 \tag{29a}$$

and

$$\epsilon_{12} = \epsilon_{21} = 0 \tag{29b}$$

in this case.

Equations (23) and (25) can be used to determine the scale dependent elastic constants $\mu_R(L)$ and $\lambda_R(L)$. For both the CA and NA algorithms, the constraint of fixed cell shape implies that $\sigma_P \equiv -1$.

IV. RESULTS

Our results for the average out-of-plane displacement squared, $\langle z^2 \rangle \equiv \langle \sum_{i=1}^{N} (z_i - z_c)^2 \rangle / N$, where z_c is the z component of the center-of-mass coordinate of the configuration, are plotted as a function of system size N in Fig. 1. Data from the constraint-Andersen, Nosé-Andersen, and Nosé-Cleveland-Wentzcovitch algorithms are indicated by circles (○), pluses (+), and squares (□), respectively. The data obtained using the CA and NA methods are in excellent agreement, and, as expected, the amplitude of the out-of-plane fluctuations is larger when the shape of the simulation cell is allowed to fluctuate. We find a scaling exponent $\zeta \approx 0.59$ for the data obtained using the CA and NA algorithms, and $\zeta \approx 0.58$ for the NCW algorithm. These results are in excellent agreement with previous simulation studies of tethered vesicles [11, 12], as well as the prediction of the self-consistent screening approximation [10].

Our data for the area susceptibility, $K_A \equiv [\langle A^2 \rangle - \langle A \rangle^2]/\langle A \rangle$, is plotted in Fig. 2. For the CA method (○), our data for the four smaller system sizes (N = 100, 196, 400, and 784) scales rather well with an exponent $\omega \approx 0.35$. This value for ω is much larger than would be obtained using the scaling relation $\omega = 2\zeta - 1$ with $\zeta = 0.59$. Note, however, that the data point for the largest system studied (N = 1600) lies well below the value extrapolated from the data for the smaller system sizes, indicating that there is probably a slow crossover to a smaller value of ω for larger systems. Our data for K_A (not shown) obtained using the NA algorithm are also consistent with those obtained using the CA method. However, the statistical errors are significantly larger; the disadvantage of the NA algorithm is that very small time steps are required in order to conserve the effective Hamiltonian and prevent a slow drift in $s(t)$. Much longer runs are therefore needed to obtain statistically significant results. While this is not a problem for strongly divergent quantities such as $\langle z^2 \rangle$, an accurate determination of the area susceptibility requires excessively long simulation runs.

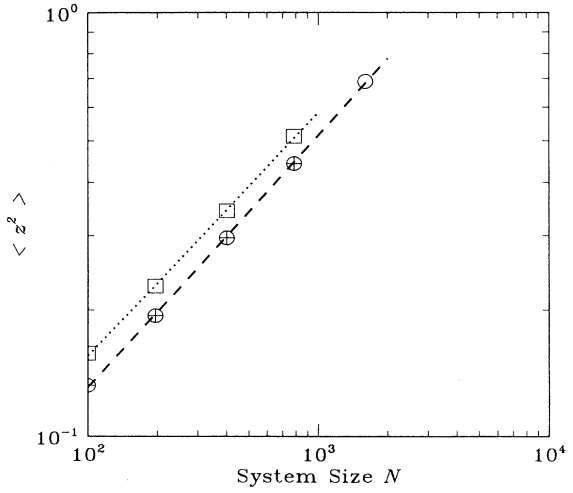

FIG. 1. $\langle z^2 \rangle$ as a function of system size N (= L^2) obtained using the CA (○), NA (+), and NCW (□) algorithms. The dashed line has a slope of 0.59. The dotted line has a slope of 0.58.

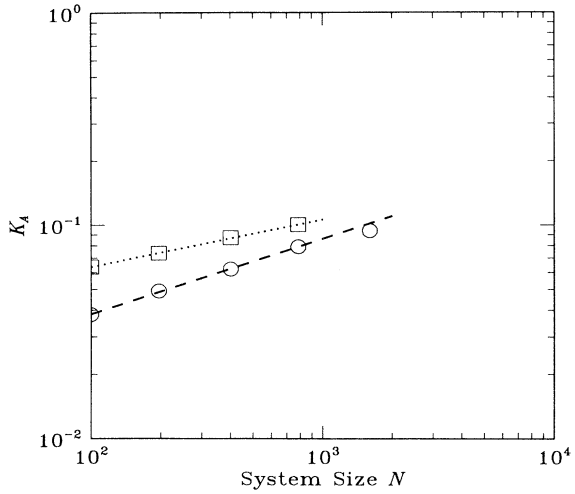

FIG. 2. Area susceptibility as a function of system size N obtained using the CA (○) and NCW (□) algorithms. The dashed line has a slope of 0.35. The dotted line has a slope of 0.22.

Results for K_A obtained using the NCW algorithm (□), with $A = \det\{\mathbf{h}\}$, are in much better agreement with the expected scaling behavior. Indeed, the data for K_A scale with an exponent $\omega \approx 0.22$; this is consistent with $\zeta \approx 0.61$, which is in quite good agreement with the value obtained from our data for $\langle z^2 \rangle$. Allowing the shape of the simulation cell to fluctuate therefore leads to a significant improvement over the Andersen method. From Fig. 2, it can be seen that systems sizes larger than $N = 1600$ are probably needed before there is a crossover to the correct scaling behavior when the shape of the simulation cell is kept fixed.

Figure 3 contains our results for the various strain correlation functions obtained using the NCW algorithm. It can be seen that our data for $\langle \epsilon_{11}\epsilon_{11} \rangle \langle A \rangle$ (○), $\langle \epsilon_{22}\epsilon_{22} \rangle \langle A \rangle$ (+), and $\langle \epsilon_{12}\epsilon_{12} \rangle \langle A \rangle$ (□) all scale with the same exponent, namely $\omega \approx 0.22$. Fits to these data yield

$$\sigma^2 \mu_R(L)/\epsilon \approx 56/L^{0.44} \tag{30a}$$

and

$$\sigma^2 \lambda_R(L)/\epsilon \approx -14/L^{0.44}. \tag{30b}$$

Note that the data for $\langle \epsilon_{11}\epsilon_{22} \rangle \langle A \rangle$ (△) do not scale nearly as well as our other data. This is due to the fact that the statistical errors are larger because the differences which need to be taken to determine this correlation function are very small. For comparison, the Lamé constants would be [24, 25]

$$\mu = \lambda \approx 126\epsilon/\sigma^2 \tag{31}$$

for a harmonic lattice with the current choice of interaction parameters.

These data can be used to obtain various estimates for the Poisson ratio. The results are shown in Fig. 4. The fact that our data for the strain correlation functions all scale with the same exponent implies that the scatter of these estimates for σ_P are of statistical origin. Our best estimate is obtained using the results for $\langle \epsilon_{11}\epsilon_{11} \rangle$, $\langle \epsilon_{22}\epsilon_{22} \rangle$, and $\langle \epsilon_{12}\epsilon_{12} \rangle$. Because of the way we calculated K_A, $\sigma_P^{(3)}$ seems to systematically overestimate the true value of the Poisson ratio for a given system size. However, these higher-order corrections vanish in the thermodynamic limit, and it can be seen that all three estimates for the Poisson ratio are converging for the larger system sizes. We feel that $\sigma_P = -0.15 \pm 0.01$ is a conservative estimate of the Poisson ratio in the infinite system size limit. This is considerably smaller in magnitude than the value predicted by the self-consistent screening approximation.

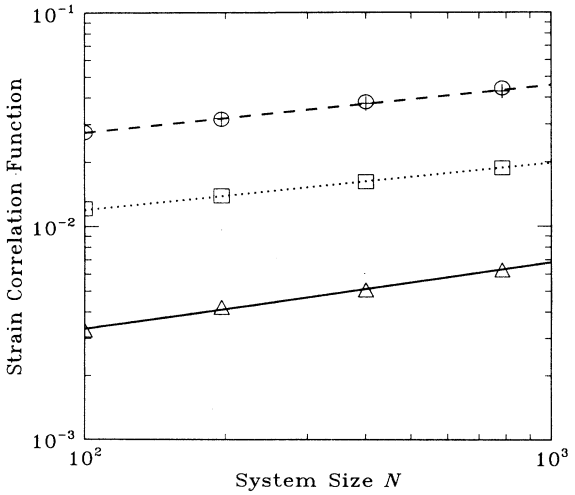

FIG. 3. Strain tensor correlation functions $\langle A \rangle \langle \epsilon_{11}\epsilon_{11} \rangle$ (○), $\langle A \rangle \langle \epsilon_{22}\epsilon_{22} \rangle$ (+), $\langle A \rangle \langle \epsilon_{12}\epsilon_{12} \rangle$ (□), and $\langle A \rangle \langle \epsilon_{11}\epsilon_{22} \rangle$ (△) as a function of system size N. The dashed and dotted lines both have the slope 0.22.

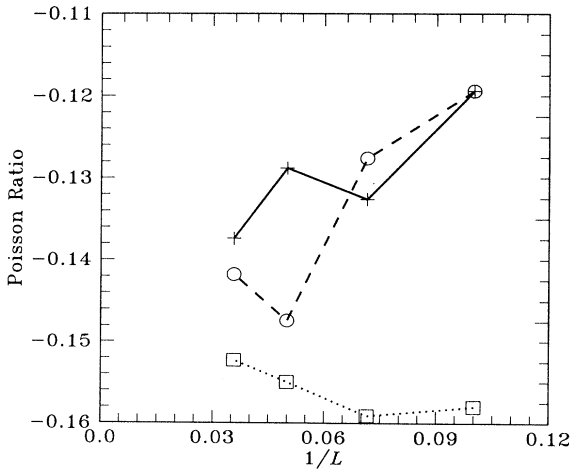

FIG. 4. Estimates for the Poisson ratio $\sigma_P = \lambda/(\lambda + 2\mu)$. $\sigma_P^{(1)} = -\langle \epsilon_{11}\epsilon_{22} \rangle / \langle \epsilon_{11}\epsilon_{11} \rangle$ (○), $\sigma_P^{(2)} = -1 + 2\langle \epsilon_{12}\epsilon_{12} \rangle / \langle \epsilon_{11}\epsilon_{11} \rangle$ (+), and $\sigma_P^{(3)} = 1 - K_A/[2\langle A \rangle \langle \epsilon_{11}\epsilon_{11} \rangle]$ (□) are plotted as functions of $1/L$, where L is the linear size of the membrane.

For the current choice of algorithms and model parameters, extremely long runs were required to obtain an accurate estimate for σ_P. In fact, it can be seen that the statistical errors are negligibly small only for the $N = 100$ particle system. For the $N = 196$ particle network, averages were taken over 2.3×10^8 time steps when determining $\langle \epsilon_{11}\epsilon_{11} \rangle$, $\langle \epsilon_{22}\epsilon_{22} \rangle$, $\langle \epsilon_{11}\epsilon_{22} \rangle$, and K_A, and 1.8×10^8 time steps for $\langle \epsilon_{12}\epsilon_{12} \rangle$. Even for such long runs, there is still a 1% difference between $\sigma_P^{(1)}$ and $\sigma_P^{(2)}$. The corresponding averages were taken over 3×10^8 and 2.5×10^8 time steps for the $N = 400$ particle network, and 1.7×10^8 and 1.2×10^8 time steps for the $N = 784$ network. The statistical errors are correspondingly larger.

V. DISCUSSION

Constant temperature-pressure MD methods have been used to determine the scaling behavior and elastic properties of tethered networks with periodic boundary conditions. In contrast with earlier published results, we find that the scaling behavior is consistent with the most accurate previous simulation studies of tethered networks. The in-plane elastic constants were also determined from the strain correlations functions, and the Poisson ratio was estimated to be $\sigma_P = -0.15 \pm 0.01$. As expected, finite size effects are much smaller than in studies of networks with free edges.

These simulations are not significantly more complicated than those of networks with free edges. Although both thermostating methods we employed yielded consistent results, Nosé thermostating in conjunction with a predictor-corrector integration scheme requires the use of extremely small integration time steps, making these simulations comparatively expensive. In contrast, the use of the Verlet algorithm with constraint thermostating, as described in Sec. II A, allowed us to use significantly larger time steps, without any loss of stability or accuracy. Using heat-bath thermostating with the velocity-Verlet algorithm for the same interaction potentials and similar interaction parameters, it is possible to use time steps Δt in the range 0.01τ–0.012τ [11, 12, 27]. Rather generally, the velocity-Verlet algorithm allows the use of time steps a factor of 2 larger than for one of the predictor-corrector algorithms [27]. With this in mind, the most efficient procedure is probably to use constraint thermostating with a Verlet algorithm. One iterative method for implementing the Verlet algorithm when there are velocity dependent forces is discussed in Ref. [26].

We now have a very complete and consistent picture of the thermal elastic and scaling behavior of tethered networks. Both the simulations described in this paper, as well as simulations of tethered vesicles [11, 12] are consistent with $\zeta = 0.59 \pm 0.02$; this result is in excellent agreement with the theoretical prediction of Le Doussal and Radzihovsky [10]. Results for the scaling behavior of the Láme constants presented in this paper are also consistent with this result. However, if the shape of the simulation cell is kept fixed (as in the Andersen algorithm), the strong supression of shear modes leads to large finite size effects in the strain correlation functions, making it impossible to determine the asymptotic scaling behavior of the Lamé constants directly for reasonable system sizes. In this context, it should be noted that we find the same scaling behavior for the Lamé constants when the original Parrinello-Rahman algorithm [20] is used instead of the Cleveland-Wentzcovitch [18, 19] algorithm. Utilizing algorithms of the type described in this paper, it is possible to essentially eliminate edge effects and obtain accurate direct estimates for the scaling behavior of both the bending rigidity and in in-plane elastic constants.

ACKNOWLEDGMENTS

This work was supported in part by National Science Foundation Center for Interfacial Engineering at the University of Minnesota, the National Science Foundation under Grant Nos. DMR-9405824 and PHY94-07194, and the donors of The Petroleum Research Fund, administered by the ACS.

[1] *Statistical Mechanics of Membranes and Surfaces*, edited by D. Nelson, T. Piran, and S. Weinberg (World Scientific, Singapore, 1989).
[2] R.R. Chianelli, E.B. Prestridge, T.A. Pecoraro, and J.P. DeNeufville, Science **203**, 1105 (1979).
[3] A. Blumstein, R. Blumstein, and H.T. Vanderspurt, J. Colloid Interface Sci. **31**, 236 (1969).
[4] C.F. Schmidt *et al.*, Science **259**, 952 (1993); A. Elgsaeter, B. Stokke, A. Mikkelsen, and D. Branton, *ibid.* **234**, 1217 (1986).
[5] S.I. Stupp, S. Son, H.C. Lin, and L.S. Li, Science **259**, 59 (1993).
[6] T. Hwa, E. Kokufuta, and T. Tanaka, Phys. Rev. A **44**, R2235 (1991); X. Wen, C. Garland, T. Hwa, M. Kardar, E. Kokufuta, Y. Li, M. Orkisz, and T. Tanaka, Nature **355**, 426 (1992).
[7] M.S. Spector, E. Naranjo, S. Chiruvolu, and J.A. Zasadzinski, Phys. Rev. Lett. **73**, 2867 (1994).
[8] J.A. Aronovitz and T.C. Lubensky, Phys. Rev. Lett. **60**, 2634 (1988); J.A. Aronovitz, L. Golubovic, and T.C. Lubensky, J. Phys. (Paris) **50**, 1787 (1989).
[9] F.F. Abraham, Phys. Rev. Lett. **67**, 1669 (1991).
[10] P. Le Doussal and L. Radzhihovsky, Phys. Rev. Lett. **69**, 1209 (1992).
[11] Z. Zhang, H.T. Davis, and D.M. Kroll, Phys. Rev. E **48**, R651 (1993).
[12] I.B. Petsche and G.S. Grest, J. Phys. (France) I **3**, 1741 (1993).
[13] H.C. Andersen, J. Chem. Phys. **72**, 2384 (1980).
[14] S. Nosé, Mol. Phys. **52**, 255 (1984).
[15] W.G. Hoover, A.J.C. Ladd, and B. Moran, Phys. Rev. Lett. **48**, 1818 (1982).

[16] A.J.C. Ladd and W.G. Hoover, Phys. Rev. B **28**, 1756 (1983).
[17] D.J. Evans, J. Chem. Phys. **78**, 3297 (1983).
[18] C.L. Cleveland, J. Chem. Phys. **89**, 4987 (1988).
[19] R.M. Wentzcovitch, Phys. Rev. B **44**, 2358 (1991).
[20] M. Parrinello and A. Rahman, Phys. Rev. Lett. **45**, 1196 (1980); J. Appl. Phys. **52**, 7182 (1981).
[21] F.F. Abraham and D.R. Nelson, J. Phys. (France) **51**, 2653 (1990).
[22] D. Brown and J.H.R. Clarke, Mol. Phys. **51**, 1243 (1984).
[23] S. Nosé, J. Chem. Phys. **81**, 511 (1984).
[24] Y. Kantor and D. Nelson, Phys. Rev. A **36**, 4020 (1987).
[25] D.H. Boal, U. Seifert, and J.C. Shillcock, Phys. Rev. E **48**, 4274 (1993).
[26] M. Ferrario and J.P. Ryckaert, Mol. Phys. **54**, 587 (1985).
[27] K. Kremer, in *Computer Simulation in Chemical Physics*, edited by M.P. Allen and D.J. Tildesley (Kluwer, Amsterdam, 1993), pp. 397–459.